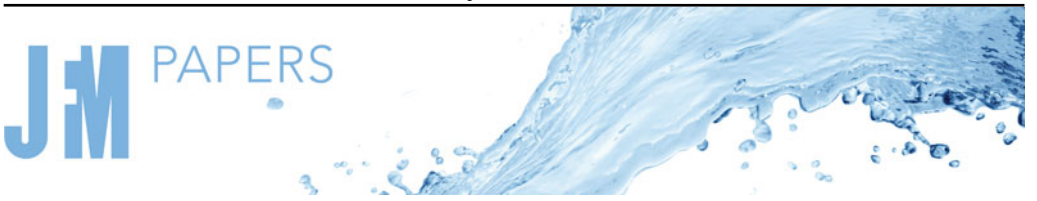
J. Fluid Mech. (2026), *vol.* 1036, A23, doi:10.1017/jfm.2026.11597



Erosion induced by a disk translating towards or away from a granular bed

Joanne Steiner[1], **Philippe Gondret**[1], **Alban Sauret**[2,3] and **Cyprien Morize**[1,4]

[1]Université Paris-Saclay, CNRS, Laboratoire FAST, F-91405 Orsay, France

[2]Department of Mechanical Engineering, University of Maryland, College Park, MD 20742, USA

[3]Department of Chemical and Biomolecular Engineering, University of Maryland, College Park, MD 20742, USA

[4]Institut Franco-Argentin de Dynamique des Fluides pour l'Environnement, CNRS (IRL 2027), Universidad de Buenos Aires, CONICET, Buenos Aires, Argentina

Corresponding author: Cyprien Morize, cyprien.morize@universite-paris-saclay.fr

(Received 30 October 2025; revised 24 February 2026; accepted 20 April 2026)

Unsteady flows generated when a body approaches or departs from a granular bed arise in swimming, burrowing, and manoeuvring devices. Yet, the threshold for grain motion in such transients remains poorly modelled due to the complexity of the flow. Building on recent characterisations of the squeeze/suction flow and vortex-ring dynamics generated by a translating disk near a rigid wall, we test how these flow scalings translate into erosion thresholds when the rigid wall is replaced by a granular bed. We report laboratory measurements of the onset of erosion when the rigid circular disk is subjected to a single vertical stroke through quiescent water above the granular bed. The stroke length and travel time were varied independently to determine the critical velocity at which the granular bed is eroded for different minimum distances from the bed. Two erosion mechanisms are observed for disk motion towards the bed: during the stroke, the outward squeezing flow erodes grains near the edge, while after stoppage, the starting vortex or associated secondary vortices impinge on the surface. For motion away from the bed, only the early interaction between the inward suction flow and the nascent vortex entrains grains. The resulting dimensionless thresholds clarify the respective roles of radial flows and vortices in transient, impulsively driven erosion.

Key words: granular media, vortex dynamics

1. Introduction

The erosion and transport of immersed granular materials subjected to a fluid flow is a fundamental and complex problem in hydraulics, coastal engineering and geomorphology.

© The Author(s), 2026. Published by Cambridge University Press.

https://doi.org/10.1017/jfm.2026.11597 Published online by Cambridge University Press

Approximately 150 years ago, the French engineer Du Boys (1879) was the first to present a rational approach to sediment transport in gravel-bed rivers, as reported by Hager (2005). In steady or statistically steady flows, the threshold is now usually characterised by a critical Shields number, Sh_c, which describes the ratio of the drag force of the fluid to the apparent weight of the particles (Shields 1936). Most studies investigating Sh_c values have been conducted in laboratory settings under uniform shear and pressure-driven current conditions (White 1940; Buffington & Montgomery 1997; Miller, McCave & Komar 1977; Loiseleux *et al.* 2005; Ouriemi *et al.* 2007). Various field observations have also validated Shields-type criteria for rivers, estuaries and desert dunes (Iversen & White 1976; Garcia 1999; Charru, Andreotti & Claudin 2013), and further laboratory investigations have highlighted the onset of bedform initiation under turbulent flows (Franklin & Charru 2011; Franklin 2015). Beyond these threshold estimates, continuum and two-phase flow models have also been developed to capture sediment transport and bedform dynamics under laminar or turbulent shear (Chauchat & Médale 2010; Charru *et al.* 2016; Chauchat *et al.* 2017).

Many natural and industrial flows are impulsive or highly unsteady, such as burst-like gusts, breaking waves, flow induced by a propeller and the vortical wake of swimming organisms. In such situations, peak shear stresses arise on the granular bed from localised, short-lived jets and vortices, which are not captured by the classical steady-flow threshold. This motivates the need for well-controlled model configurations in which the transient forcing can be characterised quantitatively and related to erosion onset.

The present study is motivated by a simple and well-defined unsteady wall-bounded flow: a disk translating normally to a nearby boundary. This kinematics generates: (i) a squeeze or suction flow in the thin gap; and (ii) starting and stopping vortices shed from the disk rim. These two flow ingredients have been quantified for a disk translating normally towards or away from a rigid wall using particle image velocimetry (PIV) and numerical simulations (Steiner *et al.* 2025). Here, we replace the rigid wall with a granular bed and ask whether these flow scalings can predict the onset, timing and spatial distribution of erosion. More broadly, this set-up captures key ingredients of many impulsive wall-bounded flows in which thin-gap radial motion and vortex shedding coexist.

Unsteady, vortex-driven erosion is important in different situations. For instance, burrowing bivalves and razor clams fluidise sand by pulsed suction flows (Winter, Deits & Hosoi 2012) and batoid fishes shed starting vortices that excavate pits for feeding or cover (Williamson & Roshko 1988). Another example is the scouring processes around obstacles such as bridge piers or offshore wind turbine masts, where the horseshoe vortices act at the foot of the structures and wake vortices act downstream, underscoring the coexistence of distinct scour modes governed by local transient vortex structures (Roulund *et al.* 2005; Manes & Brocchini 2015; Auzerais *et al.* 2016; Lachaussée *et al.* 2018).

Localised erosion and sediment resuspension by isolated vortices and transient jets have been considered in different studies. Impinging turbulent jets on a granular bed produce localised erosion when their centreline velocity exceeds a critical value (Badr, Gauthier & Gondret 2016; Brunier-Coulin, Cuéllar & Philippe 2017; Sharma *et al.* 2022), and this flow configuration is used to characterise soil stability in the so-called Jet Erosion Test (Hanson & Cook 2004). When a vortex ring hits a granular bed, it can also erode grains and create craters (Munro, Bethke & Dalziel 2009; Bethke & Dalziel 2012; Masuda *et al.* 2012; Yoshida & Sano 2014).

Another important flow configuration is encountered in footstep situations (Zhang *et al.* 2008; Kubota & Higuchi 2013), where a rapid radial outflow or inflow develops in the thin

https://doi.org/10.1017/jfm.2026.11597 Published online by Cambridge University Press

gap between the body and the bed, together with a pressure impulse and the azimuthal shear of one or more vortex rings. Human foot motions, such as walking and foot tapping, resuspend particulate matter on the floor and redistribute it, thereby increasing particle concentration in the air and affecting indoor air quality.

A closely related flow is dust resuspension during the approach and collision of an object onto a dusty wall (Mädler & Koch 1999; Eames & Dalziel 2000). The flow induced by a disk approaching a dusty wall has been investigated as a simplified model for resuspension due to human walking motion (Khalifa & Elhadidi 2007; Kubota, Hall & Higuchi 2009). These studies highlight that a high-velocity flow is ejected from the gap perimeter and spreads radially outward as a decelerating wall jet, promoting particle detachment, while a vortex structure developing outside the gap contributes to lifting and dispersing already resuspended particles (Khalifa & Elhadidi 2007; Kubota *et al.* 2009). Further studies of free-falling disks emphasise the role of near-wall shear beneath the disk rim in controlling the resuspended region (Sajadi *et al.* 2013; Elhadidi & Khalifa 2013).

Steiner *et al.* (2025) have recently performed PIV measurements and numerical simulations for the sinusoidal translation of a disk towards or away from a solid wall. This study has shown that a disk approaching a solid bottom wall drives an outward squeezing flow in the disk–wall gap that is maximum at the edge of the disk and that occurs during the decelerating part of the disk motion. In the opposite case, where the disk moves away from the solid wall, the inward suction flow in the disk–wall gap is maximum with the same velocity value, but occurs during the accelerating part of the disk motion. In both cases, the vortices are reinforced by the wall compared with the unbounded case characterised by Steiner *et al.* (2023). Owing to the contrasting flow fields – and hence wall stresses – induced by a disk moving towards or away from a wall shown by Steiner *et al.* (2025), we anticipate corresponding differences in both the onset and the spatial distribution of erosion in the case where a disk approaches or moves away from the granular bed.

For reference, in steady boundary-layer configurations, classical studies report that the critical Shields number for erosion Sh_c depends on the flow regime, with values in laboratory settings ranging from $Sh_c \simeq 0.13 \pm 0.01$ in the laminar regime to typically 0.04 in the turbulent regime (White 1940; Miller *et al.* 1977; Buffington & Montgomery 1997; Loiseleux *et al.* 2005; Ouriemi *et al.* 2007). In addition, recent experiments show that the transition to sediment transport can be 'blurred' by turbulent fluctuations, with the density of grains transported downstream that does not vanish sharply at a well-defined Sh_c (Salevan *et al.* 2017). Instead, a cross-over region is found somewhere below at $Sh_c \simeq 0.02$, as also reported by Lajeunesse, Malverti & Charru (2010).

In the present study, we report experimental measurements of the erosion threshold for a granular bed subjected to an unsteady flow induced by a translating parallel disk in both directions towards and away from the bed. The paper is organised as follows. Section 2 details the experimental apparatus, the varying control dimensional parameters and the dimensionless control parameters, as well as the experimental methods for determining the critical velocity at which the first grains get eroded and the phenomenology of what is observed. Section 3 considers the erosion in the gap between the disk and the granular bed induced by the radial squeezing or suction flow from the approaching or leaving disk, while § 4 characterises the erosion from vortices after the approaching disk motion has stopped. In all cases, we rationalise our experimental findings with the scalings outlined by Steiner *et al.* (2025) for both the radial squeezing/suction flow and the vortex flow. Section 5 summarises the main findings and outlines remaining questions.

https://doi.org/10.1017/jfm.2026.11597 Published online by Cambridge University Press

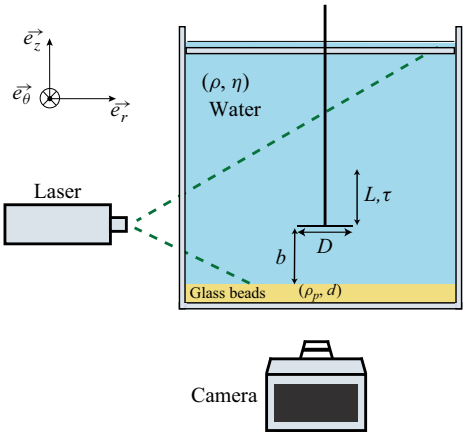


Figure 1. Schematic of the experimental set-up: a rigid disk of diameter D translates vertically over a stroke L in time τ, either descending to the minimum gap b or ascending from it.

2. Experimental methods

2.1. *Experimental set-up*

A schematic of the experimental set-up is shown in figure 1. This set-up has been used in previous studies of fluid flows around a translating disk (Steiner *et al.* 2023, 2025). In summary, the experiments were performed in a square glass tank (side 40 cm and height 60 cm) with the water level set to 40 cm. A transparent acrylic lid was placed a few millimetres beneath the free surface to suppress surface waves. At the bottom, a 1 cm thick, horizontally levelled bed of glass beads (mean diameter $d \simeq 250 \pm 50\,\mu$m, density $\rho_p = 2500\,\mathrm{kg\,m^{-3}}$) was prepared. Before each erosion experiment, the surface was smoothed with a straight edge to ensure a repeatable packing and a flat surface. While we do not measure the exact packing fraction for each preparation, we estimated the practical reproducibility of the bed preparation by repeating some threshold measurements under the same control parameters, and the resulting standard deviation of the measured critical velocity of the disk at the onset of erosion is typically 5 %–10 %, which includes the variability due to bed preparation.

A circular rigid PVC disk with a diameter $D \in [5,\ 15]$ cm, small enough compared with the tank dimensions so that lateral wall effects remain negligible and with a small thickness $e = 2$ mm ($e/D \leqslant 0.04$), was attached to a vertical shaft (1 cm diameter) driven by an AC servomotor (ECMA-C20807RS, Delta Electronics). An eccentric cam converts the continuous rotation of the motor into a sinusoidal translation of the vertical shaft. The stroke length L has been varied here in the range $2 \leqslant L \leqslant 5.2$ cm, and the minimum distance b between the disk and the granular bed in the range $0.2 \leqslant b \leqslant 2$ cm.

Throughout this study, the motion of the disk is a single translation over the time τ, during which the servomotor performs half a revolution at constant angular velocity π/τ, so that the disk accelerates and decelerates sinusoidally. The disk therefore travels the prescribed distance L in a time τ and then comes to rest. Introducing the dimensionless time $t^* = t/\tau$, the prescribed vertical position h and velocity V of the disk are

$$h(t^*) = b + \frac{L}{2}\left[1 \mp \cos(\pi t^*)\right], \quad V(t^*) = \pm V_m \sin(\pi t^*), \quad 0 \leqslant t^* \leqslant 1, \tag{2.1}$$

https://doi.org/10.1017/jfm.2026.11597 Published online by Cambridge University Press

L (cm)	D (cm)	L/D	b/D	Symbols
2	10	0.2	0.02–0.2	●
2.8	10	0.28	0.02–0.2	●
3.6	10	0.36	0.02–0.2	●
4.4	10	0.44	0.02–0.2	●
5.2	10	0.52	0.02–0.2	●
2.8	5	0.56	0.04–0.4	♦
2.8	7.5	0.37	0.027–0.27	▲
2.8	12.5	0.22	0.016–0.16	▼
2.8	15	0.19	0.013–0.13	■

Table 1. Ranges of the parameters L and D explored in the different sets of experiments together with the corresponding symbols used in the figures.

with $V_m = \pi L/(2\tau)$ the maximum translational velocity at mid-stroke $L/2$ and mid-time $t^* = 1/2$. The upper (respectively lower) sign applies when the disk starts from the bottom (respectively top) position.

The parameter ranges explored across all experiments are summarised in table 1, along with the corresponding data symbols used in the figures. The first five sets of experiments correspond to the same disk diameter, $D = 10$ cm, with different stroke lengths, L, and the data will be represented by different-coloured circles. The last four sets of experiments, together with the second set, correspond to different D values for the same $L = 2.8$ cm, and the data will appear as blue symbols of different shapes.

2.2. *Control parameters and non-dimensional groups*

The problem is fully characterised by the geometric and kinematic parameters (D, L, b, V_m) of the disk motion, the density ρ and dynamic viscosity η of the fluid, and the grain parameters (ρ_p, d) together with the gravitational acceleration g. Thus, the six following independent dimensionless parameters can be considered:

$$Re_D = \frac{\rho\, V_m\, D}{\eta}, \quad \frac{L}{D}, \quad \frac{b}{D}, \quad \frac{\Delta\rho}{\rho}, \quad Ar = \frac{\rho\, \Delta\rho\, g\, d^3}{\eta^2}, \quad Sh = \frac{\rho V_m^2}{\Delta\rho\, g\, d}, \tag{2.2}$$

where $\Delta\rho = \rho_p - \rho$ is the grain-fluid density difference. In the present study, the density ratio is constant at $\Delta\rho/\rho \simeq 1.5$ with $\rho = 10^3\ \mathrm{kg\,m^{-3}}$ the density of water. The Archimedes number $Ar \simeq 230$ indicates that grain settling occurs in the inertial regime. The remaining dimensionless groups cover the following ranges: with $\eta = 10^{-3}$ Pa s the dynamic viscosity of water, the Reynolds number Re_D spans $10^3 \lesssim Re_D \lesssim 10^5$, the relative stroke of the disk lies within $0.19 \lesssim L/D \lesssim 0.56$, the normalised gap b/D ranges from 0.013 to 0.4, and the Shields number Sh based on the driving fluid inertial forces varies approximately in the range $10^{-2} \lesssim Sh \lesssim 10^2$. The range of Re_D ensures that the disk-generated vortical flow is mostly in the inertial regime, while the broad variation of b/D together with the variation of L/D allows us to investigate the respective roles of the different flow features on the erosion threshold.

2.3. *Determination of the erosion threshold*

Two complementary procedures were used to identify the onset of erosion of the granular bed. First, direct visualisation was employed: for a set of control parameters (L, D, b), the disk velocity V was increased by decreasing the translation time τ. The threshold of erosion corresponds to the critical value τ_c at which the very first grains were observed to

https://doi.org/10.1017/jfm.2026.11597 Published online by Cambridge University Press

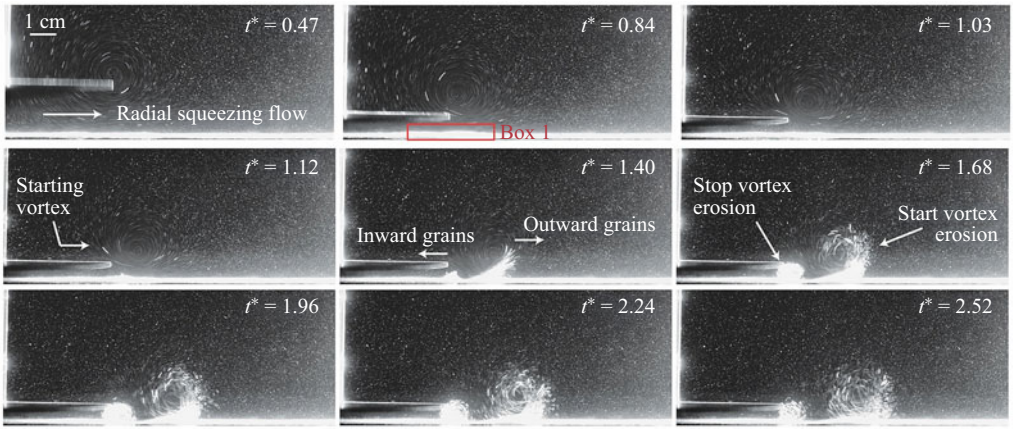


Figure 2. Pictures taken at nine successive dimensionless times $t^* = t/\tau$ illustrating the erosion of a granular bed induced by the flow generated when a disk of diameter $D = 10$ cm translates along the stroke length $L = 2.8$ cm during the travel time $\tau \simeq 0.21$ s down to the minimum/final gap distance $b = 0.5$ cm from the granular bed ($V_m = 21$ cm s$^{-1} \simeq 2V_m^c$).

be eroded from the bed. The corresponding maximum velocity $V_m^c = \pi L/(2\tau_c)$ is taken as the erosion threshold. Each erosion threshold was measured three times in independent experiments, and the resulting standard deviation of the critical velocity was typically approximately 5 %–10 %.

A second method used relied on laser profilometry: the threshold was defined as the smallest V_m for which the mean depth change exceeded 10 % of the initial layer thickness. Although the absolute values obtained by the two methods differed slightly, they are consistent for comparative purposes. Erosion thresholds generated by the radial flow before the disk stops (during both approach and retreat) were determined by direct visualisation in §§ 3.1 and 3.2, whereas the laser-profilometry criterion was applied exclusively in § 4 to the vortex-driven erosion that develops after the disk has stopped, whose strongly unsteady and fluctuating nature precludes a reliable threshold from instantaneous images.

2.4. *Phenomenology*

Figure 2 presents a time-lapse sequence from an experiment performed well above the erosion threshold, illustrating the two distinct mechanisms by which erosion arises when the disk moves downward.

The first mechanism occurs when erosion takes place while the disk is still moving ($t^* < 1$). As the disk approaches the bed, the fluid trapped beneath is expelled radially. The resulting outward radial flow, confined in the thin gap, shears the grains near the edge of the disk where the velocity is the largest (Steiner *et al.* 2025). Here, between $t^* \simeq 0.4$ and $t^* \simeq 1$, a small ridge forms at $r \simeq D/2$ (see Box 1 in figure 2 at $t^* = 0.84$) and drifts outward, revealing that only a narrow annulus of grains is eroded while the disk is in motion. At the same instant, the starting vortex is already visible in the wake of the disk, but its core is sufficiently far from the bed for the outward flow beneath the disk to remain predominantly radial and axisymmetric. Therefore, the first erosion threshold is governed by the wall shear generated by this squeezing flow in the gap.

The second mechanism is through vortex-driven erosion after the disk stops ($t^* > 1$). Indeed, once the stroke ends, the starting vortex detaches, flows around the disk and

https://doi.org/10.1017/jfm.2026.11597 Published online by Cambridge University Press

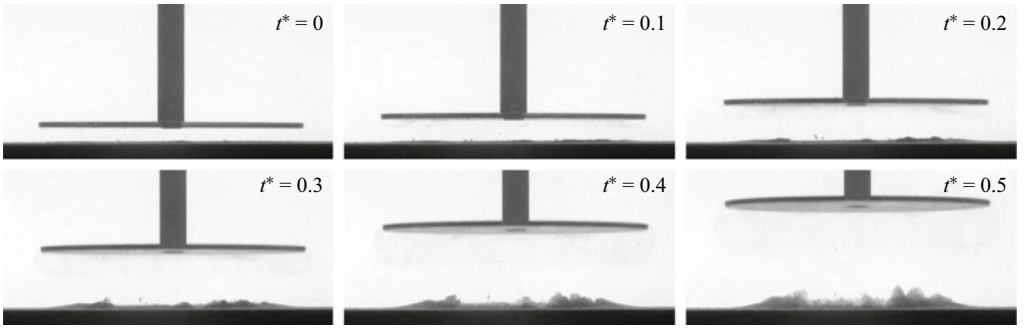


Figure 3. Time lapse showing the erosion of the granular bed produced by the unidirectional upward translation over the stroke length $L = 5.2$ cm and time $\tau \simeq 0.4$ s of a disk of diameter $D = 10$ cm starting from its minimal position $b = 0.5$ cm during the first accelerating phase ($0 \leqslant t^* \leqslant 0.5$) up to the disk velocity $V_m = 20$ cm s^{-1} $\simeq 2.5 V_m^c$.

impinges on the bed. The interaction of this vortex with the edge of the disk detaches a counter-rotating stopping vortex. Together, they form a dipole that translates parallel to the surface of the granular bed. In the present example, from $t^* = 1.12$ to 1.68, grains are entrained simultaneously outward by the starting vortex and inward by the stopping vortex, producing the bidirectional transport highlighted in the panels at $t^* = 1.40$ and 1.68. The amount of suspended granular material grows until the vortices weaken, and by $t^* = 2.52$, they can no longer sustain the grains in suspension, which then resettle onto the bed. Because the circumferential velocities in the starting and stopping vortex after the disk stops are comparable and larger than the outward flow velocity before the disk stops, the erosion mechanism by the impact of a vortex ring dipole typically imposes a higher wall stress than the squeezing radial flow. It therefore controls a separate and smaller erosion threshold.

When the disk moves away from the granular bed, a single erosion mechanism is observed, as the initial vortex ring forms beneath the translating disk and therefore never impinges directly on the bed. The erosion threshold associated with the resulting radial inflow is nevertheless modified compared with the approaching-disk case, as the confined vortex increases both radial inflow and wall shear stress.

A representative experiment is shown in figure 3, where the disk velocity is set well above the critical value V_m^c, allowing each stage to be clearly visible during the disk motion ($0 < t^* < 1$). At the very early time $t^* = 0.1$, a few grains already start to lift off, forming a mound near the granular bed. As time progresses, even more grains are entrained. They move mainly upward and inward, driven by the combined action of the inward radial flow that feeds the widening gap and the starting vortex in the wake of the disk. Because this suction flow is established as soon as the vortex begins to form, erosion is observed very early in the stroke. The deformation of the bed remains almost axisymmetric and relatively shallow compared with the erosion pattern generated when the disk approaches the bed.

In summary, when the disk moves towards the bed, the transient erosion arises first from the shear induced by the outward squeezing flow in the gap and then, if the disk stops sufficiently close to the bed, from the following impact of the starting–stopping vortex pair. When the disk moves away from the granular bed, a single erosion mechanism is observed, due to the radial inward suction flow in the gap, as the initial vortex ring forms beneath the translating disk and therefore never impinges directly on the bed.

In the following, we quantify the different erosion thresholds and describe how they scale with the governing parameters.

https://doi.org/10.1017/jfm.2026.11597 Published online by Cambridge University Press

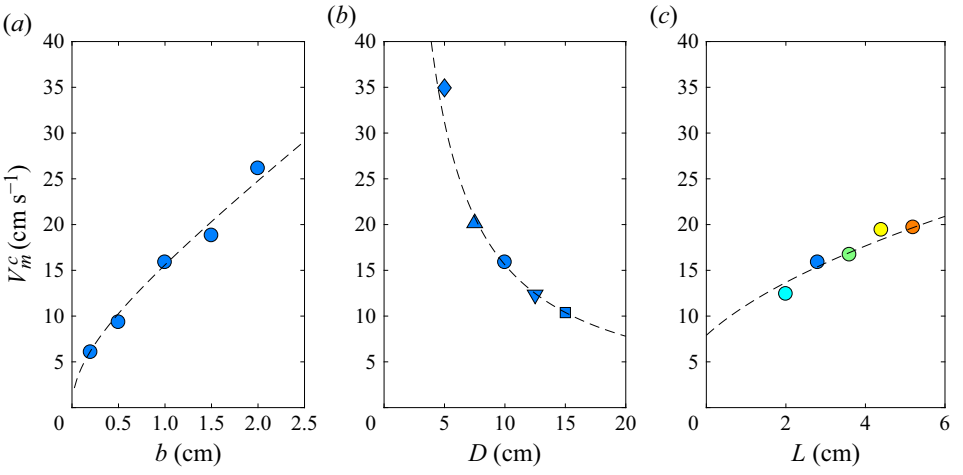


Figure 4. Critical velocity V_m^c of the approaching disk at the onset of erosion measured before the disk stops ($t^* < 1$) for a disk translating towards the granular bed as a function of (*a*) the minimal/final distance from the granular bed b for $L = 2.8$ cm and $D = 10$ cm, (*b*) the disk diameter D for $L = 2.8$ cm and $b = 1$ cm, and (*c*) the stroke length L for $D = 10$ cm and $b = 1$ cm. Dashed lines are the best fits from (3.1) corresponding in CGS units to (*a*) $V_m^c = 8b\sqrt{1 + 2.8/b}$, (*b*) $V_m^c = 156/D$ and (*c*) $V_m^c = 7.9\sqrt{1 + L}$, so that (*a*) $U_m^c = 19.75$ cm s^{-1}, (*b*) $U_m^c = 20.0$ cm s^{-1} and (*c*) $U_m^c = 19.75$ cm s^{-1}.

3. Erosion from squeezing or suction flow in the disk-bed gap

3.1. *Erosion threshold by the radial squeezing flow of a disk moving towards a granular bed*

When the disk moves towards the granular bed, the fluid confined in the narrow gap is expelled radially. The associated shear can erode the granular bed before the disk comes to a stop. We quantify here the critical disk velocity V_m^c corresponding to the first onset of erosion and demonstrate how it depends on the control parameters.

Figure 4(*a–c*) reports the values of V_m^c obtained by progressively increasing the imposed stroke velocity until a few grains begin to be eroded and transported radially outwards when the parameters b, D and L are varied separately. The critical velocity V_m^c is found to increase with the final gap b (figure 4*a*), decreases with increasing disk diameter D (figure 4*b*) and increases with the stroke length L (figure 4*c*). These trends directly reflect the way the radial flow required to conserve mass in the gap varies with the three parameters. To develop a scaling law using the maximum radial velocity, Steiner *et al.* (2025) assumed that the gap thickness $h(t)$ remains small compared with D. Then, the incompressibility condition leads to a gap-averaged radial velocity profile U that is maximum at $r = D/2$. The maximum value over time is $U_m = V_m(D/4b)(1 + L/b)^{-1/2}$, where V_m is the maximum disk velocity during the translation of the disk. The shear at the granular bed required for erosion is directly related to the radial flow and thus to U_m. Assuming that the critical value U_m^c for the gap-averaged radial velocity should remain constant for a given size and density of grains, the critical disk velocity V_m^c can be written as

$$V_m^c = U_m^c \, \frac{4b}{D} \sqrt{1 + \frac{L}{b}}. \tag{3.1}$$

Dashed lines in figure 4 show the $V_m^c(b, D, L)$ best fits of the data from (3.1) that give very close fitting values for U_m^c. The very good fit of the data for the corresponding set of

https://doi.org/10.1017/jfm.2026.11597 Published online by Cambridge University Press

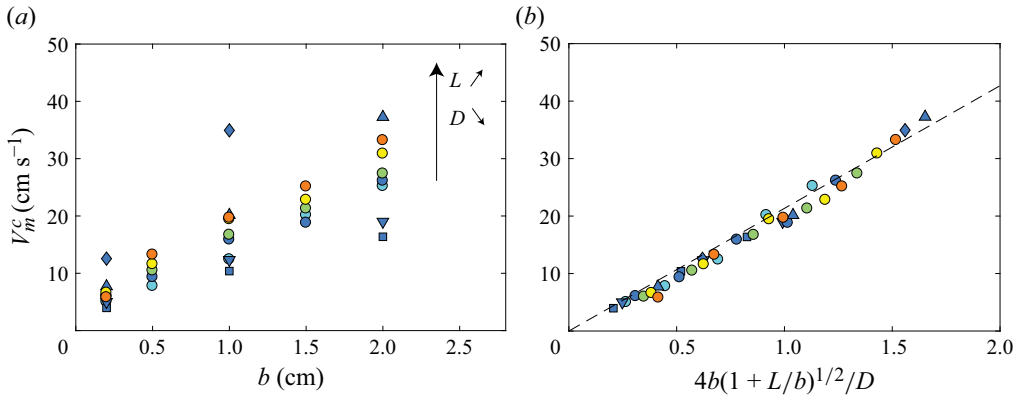


Figure 5. Critical velocity of the approaching disk at the onset of erosion by the radial outflow before the disk stops ($t^* < 1$), V_m^c, as a function of (a) the minimum distance b and (b) the parameter $4b\sqrt{1 + L/b}/D$. The dashed line corresponds to the best fit of the data by (3.1) with $U_m^c = 21.3$ cm s^{-1}.

parameters, shown in figure 4, suggests that the measured erosion thresholds should obey this relationship.

The critical disk velocity V_m^c required to dislodge the very first grains for all stroke lengths L, disk diameters D and final gaps b explored here with the colour code given in table 1 is shown in figure 5(a). The observed global trend again shows that V_m^c increases with b, indicating that a wider gap weakens the outward radial flow and requires a faster stroke for the shear at the granular bed to reach the erosion threshold. To account for the combined influence of L, D and b on the measured thresholds, the critical disk velocity V_m^c is now plotted as a function of $4b\sqrt{1 + L/b}/D$ in figure 5(b). All data collapse remarkably well onto a linear master curve as predicted from (3.1) with the fitted value $U_m^c = (21.3 \pm 2.2)$ cm s^{-1}. Thus, figure 5(b) demonstrates that the first erosion mode – driven solely by the outward squeezing flow before the disk stops – is fully captured by this gap-averaged kinematic model.

While the collapse in figure 5(b) shows that the gap kinematics predicts the erosion threshold through the maximum gap-averaged velocity U_m, this velocity is not the standard quantity used to characterise sediment mobilisation. To connect with the sediment-transport literature, and to compare the approaching and leaving cases on the same basis, we next seek an estimate of the near-bed shear associated with the squeezing flow. Since the onset of particle motion is known to be sensitive to the structure of the near-wall region and to velocity fluctuations (Quibeuf, Charru & Lacaze 2020), we examine the smooth-wall DNS of Steiner *et al.* (2025) to characterise the velocity field near the wall. Figure 6(a) shows the vertical profile of the radial velocity $u(z)$ across the gap h at the disk rim $r = D/2$ and at the dimensionless time $t^* = 0.76$, where and when U_m reaches its maximum. The profile exhibits a nearly uniform core flow together with strong velocity gradients confined to thin regions adjacent to the disk and to the wall. This is expected as the corresponding gap Reynolds number, $Re_b = \rho U_m b/\eta$, is much larger than unity, in the range $4 \times 10^2 \lesssim Re_b \lesssim 4 \times 10^3$ at the erosion threshold.

In that reference configuration, the wall shear stress is unambiguously defined from the local velocity gradient at the wall, $\tau_w = \eta(\partial u/\partial z)_{z=0}$, from which we compute the friction velocity $u_\tau = (\tau_w/\rho)^{1/2}$. For the case shown in figure 6, this gives $u_\tau = 8.5$ mm s^{-1} and a viscous length $\delta_v = \nu/u_\tau = 0.12$ mm, so that $\delta_v/d \simeq 0.5$. The profile plotted in figure 6(b) further shows a linear variation of u^+ with z^+ close to the wall, which is consistent with the presence of a viscous near-wall region in the DNS.

https://doi.org/10.1017/jfm.2026.11597 Published online by Cambridge University Press

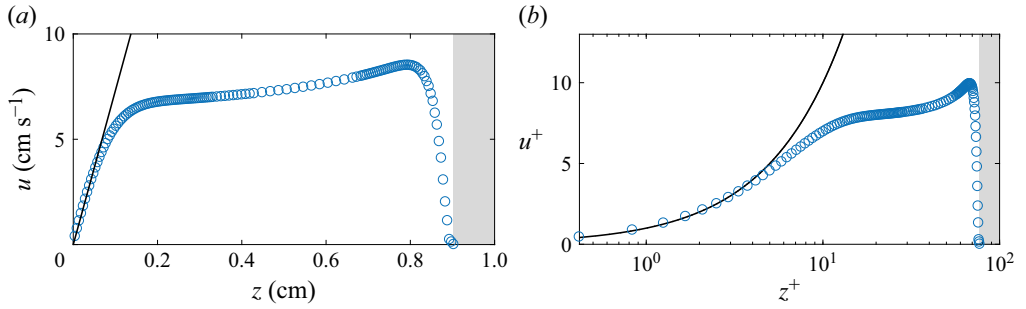


Figure 6. (*a*) Velocity profile $u(z)$ across the gap between the approaching disk ($z = h$) and the wall ($z = 0$), sampled at the disk edge ($r = D/2$) at the dimensionless time $t^* = 0.76$ where and when the fluid velocity U_m^c is maximum, for $L = 2.8$ cm, $D = 10$ cm, $b = 0.5$ cm and $\tau = 1.25$ s ($Re \simeq 3.5 \times 10^3$). The data (○) are obtained from the numerical simulations of Steiner *et al.* (2025). The shaded region corresponds to the location of the disk. The solid line is $u = 73.1z$ corresponding to $u_\tau = 8.5$ mm s^{-1} and $\delta_v = 1.2 \times 10^{-4}$ m. (*b*) Corresponding dimensionless velocity profile in wall units $u^+ = u/u_\tau$ as a function of $z^+ = z/\delta_v$. The solid line is $u^+ = z^+$.

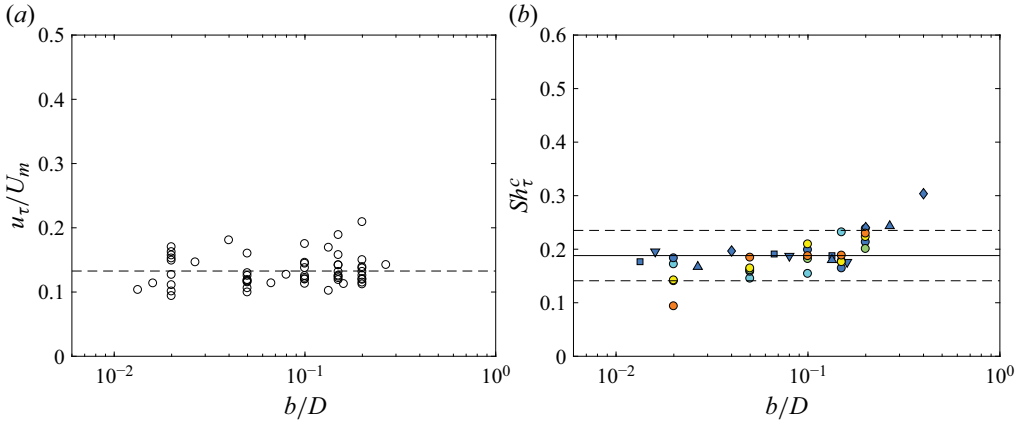


Figure 7. (*a*) Velocity ratio u_τ/U_m as a function of the dimensionless gap b/D, obtained from the numerical simulations of Steiner *et al.* (2025). The horizontal dashed line corresponds to the mean value $u_\tau/U_m \simeq 0.133$. (*b*) Friction-based Shields number Sh_τ^c defined from the friction velocity u_τ at the erosion threshold plotted as a function of b/D. The solid line marks the mean value $Sh_\tau^c \simeq 0.19$, while the dashed lines indicate a ± 25 % deviation from this mean.

The friction velocity u_τ is compared with the vertically averaged gap velocity U_m for all relative disk–wall gaps b/D in figure 7(*a*). The ratio u_τ/U_m remains approximately constant, with a mean value 0.13 ± 0.04, which provides a practical conversion between the gap-averaged velocity and the corresponding smooth-wall estimate of the near-bed shear. Since the onset of particle motion is known to be sensitive to the structure of the near-wall region and to velocity fluctuations (Quibeuf *et al.* 2020), we use u_τ here as a smooth-wall estimate of the near-bed shear associated with the radial squeezing flow. On this basis, we define a friction-based Shields number

$$Sh_\tau = \frac{\rho {u_\tau}^2}{\Delta \rho g d}. \tag{3.2}$$

Using the approximately constant ratio u_τ/U_m obtained from the smooth-wall DNS, the corresponding critical values Sh_τ^c remain nearly constant around 0.19 ± 0.05 over the explored range of b/D, as shown in figure 7(*b*). This value may be interpreted as

https://doi.org/10.1017/jfm.2026.11597 Published online by Cambridge University Press

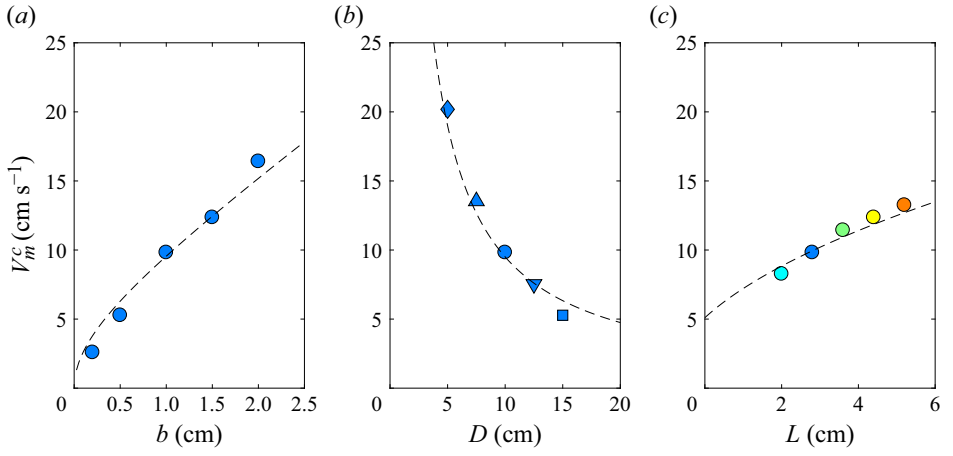


Figure 8. Critical disk velocity at the onset of erosion, V_m^c, for a disk starting from its lower position as a function of (*a*) the minimum distance to the granular bed, b ($L = 2.8$ cm, $D = 10$ cm), (*b*) the disk diameter, D ($L = 2.8$ cm, $b = 1$ cm) and (*c*) the stroke length, L ($D = 10$ cm, $b = 1$ cm). Dashed lines are best fits from (3.1) corresponding in CGS units to (*a*) $V_m^c = 4.9b\sqrt{1 + 2.8/b}$, (*b*) $V_m^c = 97/D$ and (*c*) $V_m^c = 5.1\sqrt{1 + L}$, so that (*a*) $U_m^c = 12.25$ cm s^{-1}, (*b*) $U_m^c = 12.44$ cm s^{-1} and (*c*) $U_m^c = 12.75$ cm s^{-1}.

an effective threshold for the present transient and spatially non-uniform configuration. For reference, it is of the same order as critical Shields numbers reported for steady homogeneous flows by Loiseleux *et al.* (2005) and Ouriemi *et al.* (2007), but such a comparison is only qualitative since the present threshold is inferred from smooth-wall DNS and not measured directly over a granular rough bed. This comparison with the classical Shields curve should thus be treated with care. Here, the forcing is transient, spatially non-uniform and strongly unsteady. As a result, the threshold may depend not only on the peak stress, but also on the duration over which it remains, which makes direct comparisons with steady Shields data difficult. These points can likely explain why the values of Sh_τ^c of order 0.1–0.2 are slightly higher than in the classical situation.

In summary, the erosion driven by the radial squeezing flow is set by the critical gap-averaged radial velocity $U_m^c \simeq 21$ cm s^{-1} corresponding to the critical friction velocity $u_\tau^c \simeq 2.8$ cm s^{-1} for the present glass beads. Introducing the Shields numbers based on the radial squeeze velocity U_m^c and on the friction velocity u_τ^c respectively as

$$Sh_{SQ}^c = \frac{\rho\, {U_m^c}^2}{\Delta\rho\, g\, d} \quad \text{and} \quad Sh_{\tau_{SQ}}^c = \frac{\rho\, {u_\tau^c}^2}{\Delta\rho\, g\, d}, \tag{3.3}$$

we obtain the critical values $Sh_{SQ}^c \simeq 11$ and $Sh_{\tau_{SQ}}^c \simeq 0.19$. These results provide a reliable predictive criterion for design situations where rapid gap compression mobilises sediment.

3.2. *Erosion threshold by the radial suction flow of a disk moving away from a granular bed*

The measured disk velocity V_m^c for the onset of erosion for a disk that starts from its lower position b and therefore moves away from the granular bed is reported in figure 8(*a–c*) when each parameter b, D or L is varied separately. We observe that V_m^c: (i) increases with the minimum gap distance b (figure 8*a*); (ii) decreases with increasing disk diameter D (figure 8*b*); and (iii) increases with the stroke length L (figure 8*c*). These trends are similar to those obtained when the disk moves towards the bed, yet the absolute values are systematically lower, showing that erosion is more easily triggered when the disk moves

https://doi.org/10.1017/jfm.2026.11597 Published online by Cambridge University Press

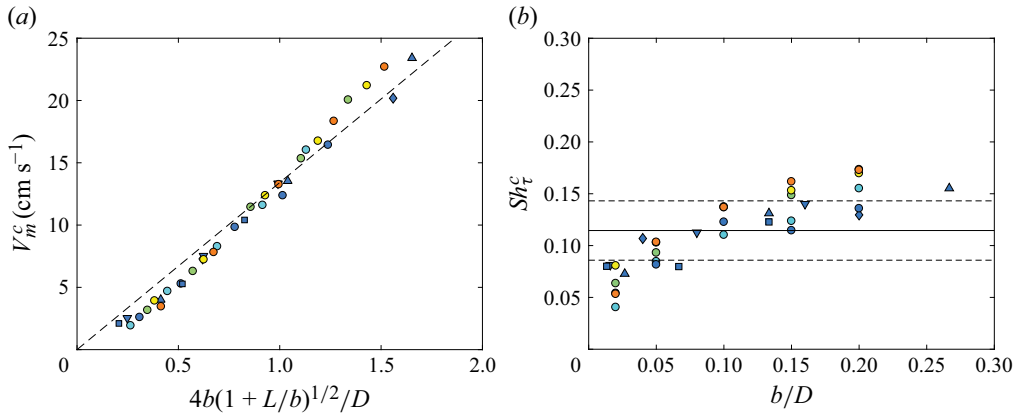


Figure 9. (*a*) Critical disk velocity at the onset of erosion, V_m^c, as a function of $4b(1+L/b)^{1/2}/D$ for a disk moving away from the granular bed. The dashed line corresponds to the best fit by (3.1) with $U_m^c = 13.4$ cm s^{-1}. (*b*) Friction-based Shields number, Sh_τ^c, as a function of b/D. The solid line is the average value $\overline{Sh_\tau^c} \simeq 0.12$, while the dotted lines delimit this mean by ± 25 %.

away from the granular bed, which may be due to the vortex formation within the gap during the disk motion that contributes to erosion. Dashed lines in figure 8 show the best fits of the data using (3.1). Indeed, the same analysis performed for the squeezing flow, where the disk moves towards the granular bed, can also be applied to the present case of suction flow, where the disk moves away from the granular bed (Steiner *et al.* 2025). The good fit of the data with close-fitting values for U_m^c for the corresponding set of parameters suggests that the measured erosion thresholds should obey this relationship.

To test if the erosion threshold is only due to the radial suction flow, the measured disk velocity V_m^c at threshold is plotted in figure 9(*a*) against the theoretical gap-averaged maximum velocity given by (3.1) for all our data. All the data collapse rather well onto a master curve that is close to a linear law with a slope corresponding to $U_m^c = (13.4 \pm 1.4)$ cm s^{-1}, which is indeed significantly smaller than the value $U_m^c = (21.3 \pm 2.2)$ cm s^{-1} found in the case where the disk moves towards the granular bed. As in the previous squeeze case, the characteristic Reynolds number for the gap flow is again much larger than one, in the range $2 \times 10^2 \lesssim Re_b \lesssim 2 \times 10^3$ at the erosion threshold, so that we anticipate some possible differences in the velocity profile of the gap flow for the two cases where the disk approaches or moves away from the granular bed, and thus in the onset of erosion.

Following the same procedure as already presented, the friction velocity u_τ in the viscous sublayer is also extracted from the DNS of Steiner *et al.* (2025). Across the full range of disk–wall separations explored, the ratio of this friction velocity to the gap-averaged velocity remains essentially constant with the value $u_\tau/U_m \simeq 0.17 \pm 0.04$, which is a little larger than the value $u_\tau/U_m \simeq 0.13 \pm 0.04$ found in the case where the disk moves towards the wall. The particle Reynolds number $Re_p = u_\tau d/\nu$ is always larger than unity over the range explored. Using u_τ as a smooth-wall estimate of the near-bed shear, we again define a friction-based Shields number as $Sh_\tau = (\rho u_\tau^2)/(\Delta\rho\, g\, d)$. The corresponding critical value Sh_τ^c for bed erosion threshold is plotted as a function of the relative minimum distance of the disk to the granular bed b/D in figure 9(*b*). The mean value for this critical Shields number is $\overline{Sh_\tau^c} \simeq 0.12 \pm 0.02$. When compared with the case where the disk moves towards the granular bed, this mean value is significantly smaller and there is also a significant trend of smaller Sh_τ^c for smaller b/D, which can be observed

https://doi.org/10.1017/jfm.2026.11597 Published online by Cambridge University Press

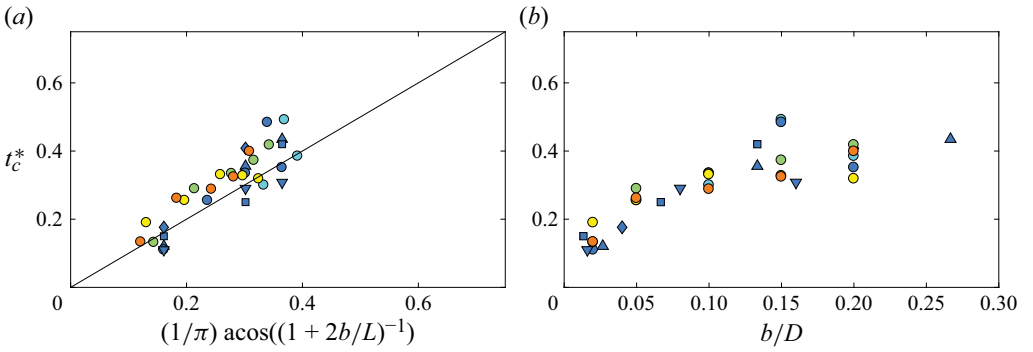


Figure 10. Dimensionless time t_c^* at which the first grains begin to move at the erosion threshold, with the disk released from its lower position, as a function of (*a*) the dimensionless time $t_m^* = (1/\pi)\mathrm{acos}(1+2b/L)^{-1}$ at which the maximum gap-averaged radial velocity U_m is predicted to occur by Steiner *et al.* (2025), and as a function of (*b*) the normalized gap b/D. The solid line corresponds to $t_c^* = t_m^*$.

despite the scattering of the data. This likely reflects that the model neglects the influence of the vortex on the gap-driven inward radial flow. This interpretation is also consistent with the onset times reported in figure 10: when the disk moves away from the bed, erosion can start early in the stroke ($t_c^* < 0.5$), i.e. before the disk reaches its maximum velocity. In that situation, a purely gap-driven estimate based on the peak U_m may under-represent the instantaneous near-bed forcing at t_c^* because the developing vortex within the gap contributes to the shear. In addition, figure 10(*b*) shows that the onset time of erosion increases significantly with b/D. This supports the hypothesis that the vortex contribution depends on the instant when erosion begins: the vortex will be more or less developed and more or less distant from the granular bed.

Figures 9(*b*) and 10(*b*) show that both the critical Shields number Sh_τ^c and the critical time t_c^* for erosion increase with b/D. Indeed, at small gaps ($b/D \lesssim 0.2$), the vortex core lies only a few grain diameters above the bed and the circumferential velocity, which decays as $1/r'$, increases the gap–driven inflow, so grains lift off almost instantly. As the gap widens, the core moves away and its contribution to the near-wall shear decays roughly as $1/b$. A larger purely gap-driven inflow is therefore needed to reach the same bed stress, which delays erosion (larger t_c^*) and raises the value of the critical Shields number $Sh_\tau^c \propto {U_m^c}^2$.

In summary, when the disk moves away from the granular bed, the erosion is triggered during the first accelerating phase of the disk motion by the radial inflow generated between the disk and the granular surface, which is reinforced by the starting vortex ring. The threshold velocity follows the same scaling law of (3.1) as in the approaching-disk case, but with a smaller prefactor. Indeed, the erosion driven by the radial suction flow is set by the critical gap-averaged radial velocity $U_m^c \simeq 13\ \mathrm{cm\ s^{-1}}$, which is 40 % smaller than the critical value $U_m^c \simeq 21\ \mathrm{cm\ s^{-1}}$ found in the approaching case. However, due to a larger u_τ/U_m ratio than in the approaching case, the critical friction velocity is $u_\tau^c \simeq 2.3\ \mathrm{cm\ s^{-1}}$, only 20 % smaller than the critical value $u_\tau^c \simeq 2.8\ \mathrm{cm\ s^{-1}}$ found in the approaching case. Considering the Shields numbers based on the radial suction velocity U_m^c and on the friction velocity u_τ^c respectively as

$$Sh_{SU}^c = \frac{\rho\, {U_m^c}^2}{\Delta\rho\, g\, d} \quad \text{and} \quad Sh_{\tau SU}^c = \frac{\rho\, {u_\tau^c}^2}{\Delta\rho\, g\, d}, \tag{3.4}$$

https://doi.org/10.1017/jfm.2026.11597 Published online by Cambridge University Press

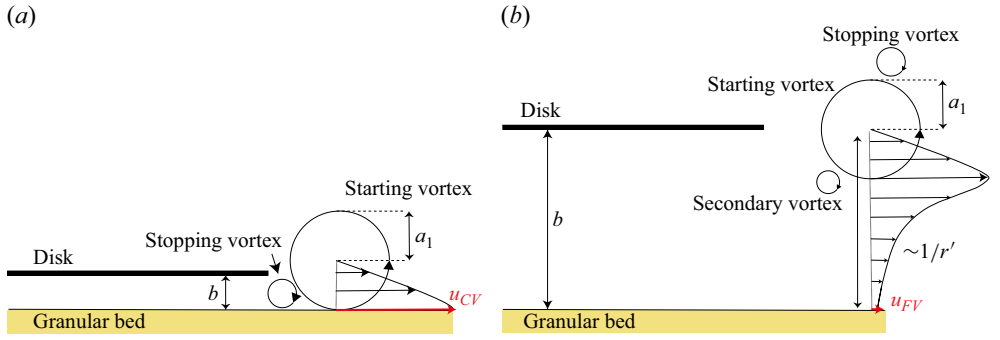


Figure 11. Schematic of (*a*) the impact of the dipole formed by the starting vortex and the stopping vortex on the granular bed when the approaching disk stops close to the bed ($b/a_1 \lesssim 1$) and of (*b*) the near-wall velocity behaviour when the disk stops farther from the bed ($b/a_1 \gtrsim 1$).

we obtain the critical values $Sh^c_{SU} \simeq 4$ and $\mathrm{Sh}^c_{\tau_{SU}} \simeq 0.12$. These results provide a reliable predictive criterion for design situations where rapid gap expansion mobilises sediment.

The fact that the critical Shields number for erosion is not strictly identical for the squeeze flow and the suction flow is due to the fact that the flow is not strictly identical for two reasons corresponding to unsteadiness. The first reason is that the maximal radial velocity U_m of the flow induced by the motion of the disk is identical in both configurations, but not the time t_m at which this maximal radial velocity is reached and, thus, not the typical flow acceleration U_m/t_m. Indeed, the time t_m is smaller in the suction flow, for which $0 < t_m < \tau/2$, than in the squeeze flow, for which $\tau/2 < t_m < \tau$. As it is typically three times smaller, with a precise value that depends slightly on b/L, the acceleration U_m/t_m is typically three times larger in the suction flow than in the squeeze flow. This larger acceleration is expected to induce a larger driving drag force on the grains from the added-mass force term, which can explain some of the difference between the two flow configurations. The second reason is the vortex flow that modifies the velocity profile within the gap and induces some additional unsteady effects.

4. Erosion by vortices

Let us now focus on the vortex erosion that may be observed after the disk stops its motion towards the granular bed, as reported in § 2.4. When the disk has completed its stroke ($t^* > 1$), the starting vortex ring, generated in its wake during the translation, drifts downward and interacts with the rim of the disk. This interaction detaches a counter-rotating stopping vortex which, together with the starting vortex, forms a dipole of vortex rings that propagates parallel to the granular bed surface, as illustrated by the schematics of figure 11. When the disk stops sufficiently close to the bed ($b/a_1 \lesssim 1$, where $a_1 = a(t^* = 1)$ is the core radius of the starting vortex at the disk stop), as illustrated in figure 11(*a*), the dipole impinges on the grains almost immediately, entraining sediment both outward for the starting vortex and inward for the stopping vortex, thus generating the bidirectional transport described in figure 2. In this regime, the disk velocity V_m is the experimental control parameter, but the relevant forcing for erosion is the near-bed velocity induced by the vortices. We thus need to introduce u_{CV} and u_{FV} (see figure 11).

When the disk stops far from the bed ($b/a_1 \gtrsim 1$), the stopping vortex flows around the starting vortex without impacting the bed directly. Therefore, erosion is delayed and results either from the slowly decaying velocity field of the starting vortex itself or from the later impact of secondary stopping vortices (figure 11*b*). These two scenarios will be referred to

https://doi.org/10.1017/jfm.2026.11597 Published online by Cambridge University Press

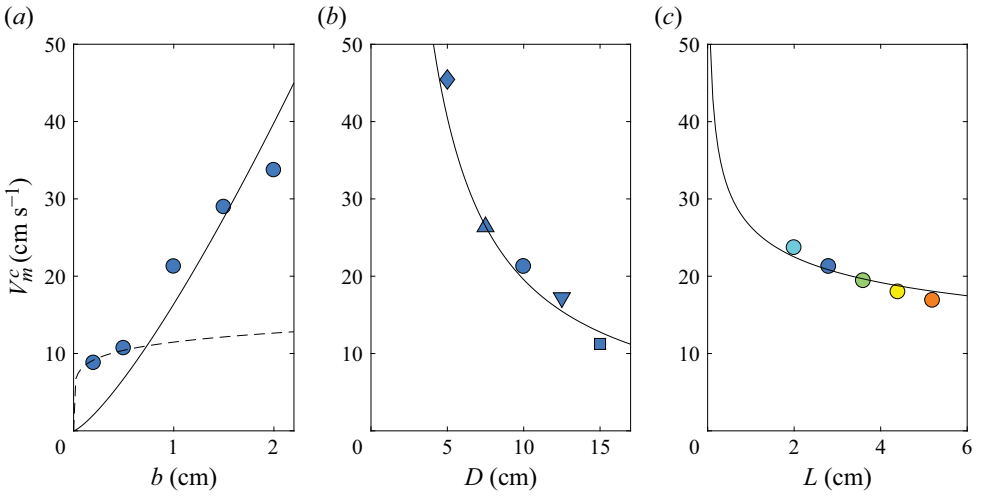


Figure 12. Critical velocity of the approaching disk at the onset of vortex erosion occurring once the disk has come to rest ($t^* > 1$), V_m^c, measured for a disk released from its upper position as a function of (*a*) the final distance to the granular bed, b ($L = 2.8$ cm, $D = 10$ cm); (*b*) the disk diameter, D ($L = 2.8$ cm, $b = 1$ cm); and (*c*) the stroke length, L ($D = 10$ cm, $b = 1$ cm). The solid lines are best fits from (4.4) corresponding in CGS units to (*a*) $V_m^c \simeq 16.4\, b^{1.28}$ (for $b > 0.8$ cm), (*b*) $V_m^c \simeq 220/D^{1.05}$ and (*c*) $V_m^c \simeq 26.4/L^{0.23}$, with (*a*) $u_{FV}^c \simeq 26$ cm s^{-1}, (*b*) 31 cm s^{-1} and (*c*) 33 cm s^{-1}. The dashed line is the best fit from (4.4) for $b < 0.8$ cm corresponding in CGS units to $V_m^c \simeq 11.5\, b^{0.14}$ with $u_{CV}^c \simeq 41$ cm s^{-1}.

as CV for the close vortex case ($b/a_1 \lesssim 1$) and FV for the far vortex case ($b/a_1 \gtrsim 1$). Thus, two distinct situations, depending on the ratio b/a_1, will be considered when analysing the erosion thresholds after the disk comes to rest.

The critical disk velocity V_m^c required to trigger vortex-driven erosion after the disk stops is reported in figure 12(*a–c*). For a fixed disk diameter D and stroke length L, V_m^c increases monotonically with the minimum distance b to the bed (figure 12*a*), meaning that a faster stroke is needed when the vortices must travel farther before hitting the grains. In contrast, V_m^c decreases with increasing disk diameter D (figure 12*b*) because the circulation of the starting vortex scales roughly with D (Steiner *et al.* 2025), so that a larger disk generates a stronger vortex for the same disk velocity. Finally, V_m^c is found to decrease with increasing stroke length L (figure 12*c*), which is opposite to what we observed for the squeezing-flow threshold discussed in the previous section. This difference can be explained by a longer acceleration phase, which allows the vortex to build up more circulation, which scales roughly with $L^{1.2}$ (Steiner *et al.* 2025), and thus leads to bed erosion at a lower disk velocity.

All the critical values V_m^c for vortex-driven erosion are shown in figure 13(*a*) as a function of the size ratio b/a_1 of the gap with the core radius a_1 of the vortex at the disk stop. There is substantial dispersion, but the global trend is that V_m^c increases with larger b/a_1. The critical dimensionless time t_c^* at which the first grains begin to be eroded just above the threshold is shown in figure 13(*b*). The data show that $t_c^* \simeq 1$ for $b/a_1 \lesssim 1.2$ and that $t_c^* > 1$ for $b/a_1 \gtrsim 1.2$, which corresponds to the CV and FV erosion scenarios where the vortex erosion arises at the disk stop or later, respectively.

To estimate the forcing and corresponding velocity near the granular bed, we consider that the shear applied by the vortices on the granular bed can be estimated by the circumferential velocity of the vortex close to the granular bed. The two following

https://doi.org/10.1017/jfm.2026.11597 Published online by Cambridge University Press

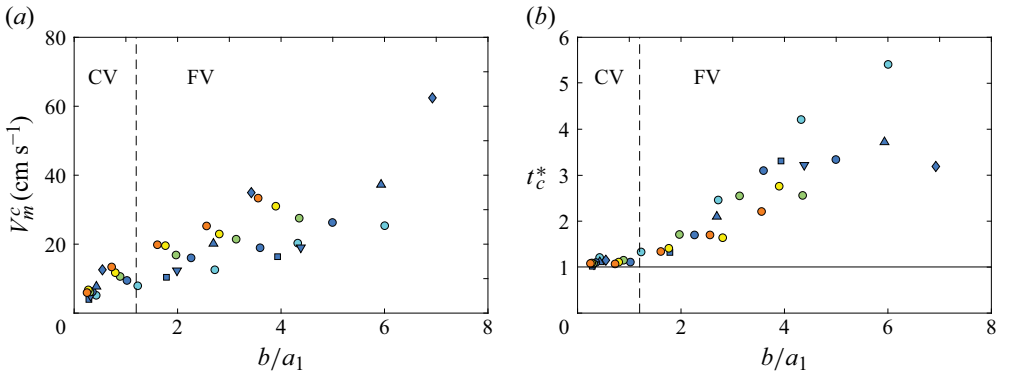


Figure 13. (*a*) Velocity of the disk at the vortex erosion threshold as a function of b/a_1. (*b*) Dimensionless time t_c^* at which the first grains begin to be eroded; the horizontal line marks the instant when the disk comes to rest. In both panels, the vertical dashed lines show the transition $b/a_1 = 1.2$ between CV and FV.

expressions are appropriate depending on the position of the vortex core at $t^* = 1$:

$$u_{CV} = \frac{\Gamma_1}{2\pi a_1}, \quad u_{FV} = \frac{\Gamma_1}{2\pi b}, \tag{4.1}$$

for $b/a_1 \lesssim 1.2$ and $\gtrsim 1.2$, respectively, where $\Gamma_1 = \Gamma(t^* = 1)$ and a_1 denote the circulation and core radius of the starting vortex at the disk stop. For $b/a_1 \lesssim 1.2$ (CV), the stopping vortex is trapped between the disk and the bed so that the dipole impinges directly on the bed, and the first expression in (4.1) therefore sets the relevant shear. When $b/a_1 \gtrsim 1.2$ (FV), the starting vortex remains at an average distance b from the grains and its $1/r'$ velocity decay controls the erosion at $r' \simeq b$, leading to the second expression in (4.1).

The circulation Γ_1 and radius a_1 of the starting vortex at the disk stop measured by Steiner (2023) and given in (A10) in Appendix A.2.1 are the following: $|\Gamma_1| \simeq 1.1\, L^{1.23} D^{1.05} b^{-0.28} \tau^{-1}$ and $a_1 \simeq 0.064\, L^{0.55} D^{0.59} b^{-0.14}$. They follow the same scalings as the maximal circulation Γ_m and radius a_m reported by Steiner *et al.* (2025) with numerical prefactors only a little smaller: 1.1 instead of 1.3 for the circulation and 0.064 instead of 0.068 for the radius, corresponding to a decrease of only 20 % and 10 %, respectively. The corresponding expressions for the velocity induced by the vortex in the vicinity of the grains, u_{CV} and u_{FV}, are thus

$$u_{CV} \simeq \frac{17\, L^{0.68}\, D^{0.46}}{2\pi\, b^{0.14}\, \tau}, \quad u_{FV} \simeq \frac{1.1\, L^{1.23}\, D^{1.05}}{2\pi\, b^{1.28}\, \tau}. \tag{4.2}$$

Note that the two scalings of (4.2) are very different. A quantitative comparison between the experimental thresholds and the theoretical predictions is provided in figure 12(*a–c*). The dashed lines denote the confined-vortex (CV) regime, in which the stopping vortex is confined between the disk and the bed; the solid lines denote the far-vortex (FV) regime, in which the far-field action of the vortex erodes the granular bed from a distance of order b. In each case, the curves represent best fits obtained from (4.2), with fitted coefficients reported in the caption of figure 12. The good agreement between experiments and the model based on (4.2) confirms the relevance of the scaling arguments for both regimes and highlights the distinct physical mechanisms controlling erosion depending on the disk–bed separation. It is worth noting that in figure 12(*a*), the first two data points correspond to the confined-vortex (CV) regime, while the remaining points fall in the far-vortex (FV) regime. By contrast, all the data shown in figure 12(*b–c*) belong to the FV regime. This distinction indicates that only when the disk stops at very small gaps does the dipole impinge directly

https://doi.org/10.1017/jfm.2026.11597 Published online by Cambridge University Press

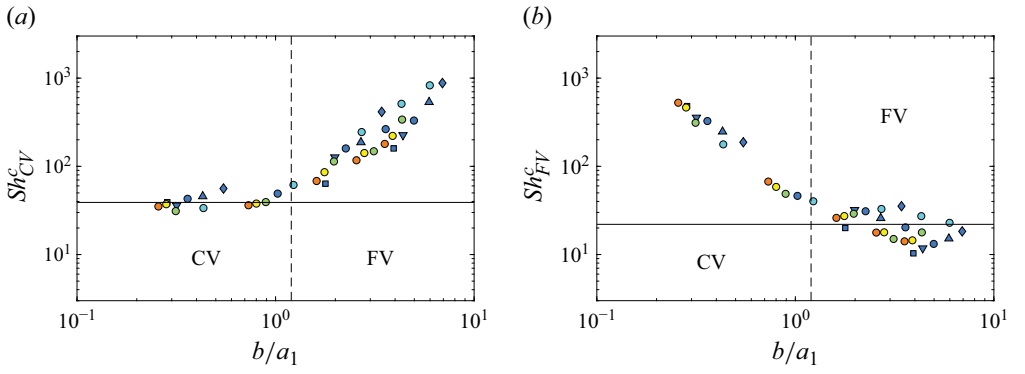


Figure 14. Critical Shields number (*a*) Sh^c_{CV} and (*b*) Sh^c_{FV} defined with the local velocity u_{CV} or u_{FV} induced by the impact of the starting vortex ring, as a function of b/a_1. The vertical dashed lines mark the transition at $b/a_1 = 1.2$, while the horizontal lines indicate the mean values $\overline{Sh^c_{CV}} = 39$ and $\overline{Sh^c_{FV}} = 22$.

on the bed (CV), whereas in most other cases, erosion is governed by the far-field action of the starting vortex (FV). The fits reported in figure 12 thus successfully discriminate between the two regimes and capture the scaling of the erosion threshold with the control parameters in both cases.

Using $u_{CV,FV}$, we can estimate the corresponding Shields number based on the local vortex-induced velocity $Sh_{CV,FV} = \rho u^2_{CV,FV}/(\Delta\rho\, g\, d)$. The critical values of these two Shields numbers Sh^c_{CV} and Sh^c_{FV} calculated from the critical time τ_c measured at the erosion threshold are reported as a function of b/a_1 in figures 14(*a*) and 14(*b*), respectively. We observe a rather good collapse of the data on the two following plateau values:

$$Sh^c_{CV} \simeq 39 \pm 15, \quad Sh^c_{FV} \simeq 22 \pm 12, \tag{4.3}$$

for $b/a_1 \lesssim 1.2$ and $b/a_1 \gtrsim 1.2$, respectively. The dispersion of the data around the plateau value $Sh^c_{CV} \simeq 39$ in figure 14(*a*) is not so large, less than 40 %. The larger dispersion – exceeding 50 % of the data around the plateau value $Sh^c_{FV} \simeq 22$ in figure 14(*b*) – is likely due to the fact that erosion may not originate from the primary starting vortex, but rather from the secondary stopping vortex or from a tertiary vortex whose circulation and core radius may slightly differ. These values of Shields numbers are relatively high because they are not based on the friction velocity, which was not measured, but the corresponding local Shields number would certainly be roughly 10^{-2} smaller. This observation confirms that erosion is governed by inertial stresses in both CV and FV scenarios, but with different characteristic velocities. The particle Reynolds number $Re_p = u_{CV,FV} d/\nu$ based on the circumferential velocity u_{CV} and u_{FV} exceeds always 80 throughout the explored parameter space, further supporting the inertial nature of the destabilising force. The critical values u^c_{CV} and u^c_{FV} at the erosion threshold corresponding to the critical Shields numbers given in (4.3) are $u^c_{CV} \simeq (38 \pm 8)$ cm s^{-1} and $u^c_{FV} \simeq (28 \pm 7)$ cm s^{-1}, respectively. Considering (4.2), one can infer the two possible scalings for the critical disk velocity $V^c_m = \pi L/(2\tau_c)$ in the CV and FV cases:

$$V^c_{m,CV} \simeq \frac{\pi^2}{17} \frac{b^{0.14}\, L^{0.32}}{D^{0.46}}\, u^c_{CV}, \quad V^c_{m,FV} \simeq \frac{\pi^2}{1.1} \frac{b^{1.28}}{D^{1.05}\, L^{0.23}}\, u^c_{FV}. \tag{4.4}$$

These scalings explain the variations of V^c_m reported in figure 12(*a–c*). Indeed, in the case of figure 12(*b*,*c*) corresponding to FV flow, the second scaling fits well the data with a decrease of V^c_m for both increasing D and L (see solid lines). For the case of figure 12(*a*), the second scaling (solid line) fits quite well the three points corresponding to large enough

https://doi.org/10.1017/jfm.2026.11597 Published online by Cambridge University Press

b values, with a roughly linear increase of V_m^c with b, whereas the first scaling (dashed line) fits well the two points corresponding to small enough b values, with a sublinear increase of V_m^c with b.

In summary, the erosion occurring after the disk stops is controlled by the impact of the vortices generated during the stroke. A single geometric parameter, the ratio b/a_1, selects whether the bed is eroded by the immediate dipole impact (CV) when the disk stops close to the granular bed ($b/a_1 \lesssim 1$) or by the subsequent far-field action of the vortex (FV) when the disk stops far from the granular bed ($b/a_1 \gtrsim 1$). When expressed in terms of the physically relevant local velocity, the critical Shields number is nearly constant within each regime, providing a criterion for vortex-driven grain motion that is independent of the disk kinematics.

5. Conclusion

In this study, we experimentally investigated how a rigid disk of diameter D translating towards or away from a granular bed can erode and ultimately resuspend glass beads. We have focused here on an elementary unsteady motion at the minimal distance b from the granular bed: a single stroke of length L during the time τ at the maximum velocity V_m, and have quantified the onset of erosion V_m^c and the dimensionless time $t_c^* = t_c/\tau$ at which it arises.

When the disk moves towards the bed, we found that the initial erosion is triggered by the maximal radial outflow that develops beneath the disk while it is still decelerating ($1/2 < t_c^* < 1$). For sufficiently small gaps ($b/D \lesssim 0.2$), the threshold is governed by a constant critical outflow velocity $U_m^c \simeq V_m^c D/[4b(1 + L/b)^{1/2}]$ that is related to the disk motion close to the granular bed from mass conservation. The critical local Shields number based on the friction velocity $u_\tau \simeq 0.13 U_m$ at the bed level is $Sh_\tau^c \simeq 0.19$. Once the disk stops, the interaction between the starting vortex ring and the edge of the disk gives rise to a dipole of vortex rings. This dipole produces either immediate ($t_c^* \simeq 1$) or delayed ($t_c^* > 1$) erosion depending on whether the dipole is close to or far from the bed, respectively, i.e. whether the ratio b/a_1 is smaller or larger than unity, respectively, where a_1 is the radius of the vortex core at the disk stop. This complex vortex flow explains both the bidirectional grain transport observed near the bed and the increase in the disk critical velocity with b/a_1.

In the opposite case, when the disk translates away from the granular bed, erosion occurs before the disk reaches its maximum velocity ($0 < t_c^* < 1/2$). As the time at which the maximal radial inflow occurs is significantly smaller than the time at which the maximal radial outflow occurs for the reverse motion, the flow acceleration is significantly larger which induces a larger driving drag force for erosion due to the added-mass contribution. Furthermore, the inward radial suction flow is reinforced by the developing starting vortex within the gap during its first accelerating phase of the disk. These two phenomena mean that the critical Shields number $Sh_\tau^c \simeq 0.12$ for the suction flow is significantly smaller than the value 0.19 for the squeeze flow.

Taken together, the two configurations highlight how asymmetries in the flow, depending on the direction of motion (outflow versus inflow, starting versus stopping vortices), result in different erosion thresholds. The asymmetry in the flow generated also explains why a disk that travels away from the granular bed, despite generating a weaker wall stress, can still mobilise grains earlier in the stroke owing to the rapid growth of the starting ring. These findings provide a quantitative framework for guiding geophysical or biological scenarios in which impulsively moving objects induce sediment transport via vortex shedding. An open issue is how the erosion and transport threshold is altered when

https://doi.org/10.1017/jfm.2026.11597 Published online by Cambridge University Press

the disk (or a biological analogue such as a flounder fin) performs repeated oscillations rather than a single stroke, because the vortices shed during successive half-cycles are expected to interact with one another in a more complex, history-dependent manner. Erosion has already yielded some surprising results for vertical oscillations of a horizontal disk (La Ragione *et al.* 2019) or the horizontal oscillations of a vertical plate (Martino *et al.* 2018) near a granular bed.

Supplementary movie. Supplementary movie is available at https://doi.org/10.1017/jfm.2026.11597.

Acknowledgements. The authors thank I. Delbende for his help in the numerical simulations, G. Quibeuf and G. Renard for their preliminary experimental contributions, and J. Amarni, A. Aubertin, L. Auffray and R. Pidoux for their work on the experimental set-up.

Declaration of interests. The authors report no conflict of interest.

Appendix A. Scalings of the starting and stopping vortices in the wake of a disk

A.1. *Vortex scalings in the unbounded case*

In the unbounded case, where the disk of diameter D is far from any boundaries ($b/a \gg 1$), the maximum circulation $|\Gamma_m|$ and core radius a_m of the starting vortex ring formed in the wake of a translating disk whose velocity evolves sinusoidally over the stroke length L and time τ have been shown by Steiner *et al.* (2023) to follow the scaling laws

$$|\Gamma_m| \simeq 2.1\, L^{4/3} D^{2/3} \tau^{-1} \quad \text{and} \quad a_m \simeq 0.1\, L^{2/3} D^{1/3}. \tag{A1}$$

The maximum circulation and core radius of the starting vortex have been reported by Steiner *et al.* (2023) to be reached at the dimensionless times $\tau^*_{\Gamma_m} = 0.70 \pm 0.02$ and $\tau^*_{a_m} = 0.79 \pm 0.07$, respectively, which do not depend on the size ratio L/D. Steiner *et al.* (2023) have also shown that the circulation and core radius of the starting vortex at the disk stop ($t^* = 1$) follow the same scaling laws with only slightly smaller numerical coefficients:

$$|\Gamma_1| \simeq 1.9\, L^{4/3} D^{2/3} \tau^{-1} \quad \text{and} \quad a_1 \simeq 0.085\, L^{2/3} D^{1/3}. \tag{A2}$$

And finally, Steiner *et al.* (2023) have also reported that the scalings of the maximum circulation and core radius of the counter-rotating stopping vortex are the same, with even smaller coefficients:

$$|\Gamma_{m,s}| \simeq 1.1\, L^{4/3} D^{2/3} \tau^{-1} \quad \text{and} \quad a_{m,s} \simeq 0.06\, L^{2/3} D^{1/3}. \tag{A3}$$

The maximum circulation and maximum core radius of the stopping vortex are thus about half the maximum values measured for the primary starting vortex. They are reached at the dimensionless times $\tau^*_{\Gamma_{m,s}} = 1.23 \pm 0.05$ and $\tau^*_{a_{m,s}} = 1.27 \pm 0.09$, respectively.

A.2. *Vortex scalings close to a wall*

In the presence of a bottom wall, the minimum distance b between the disk and the wall has been shown to play a significant role in the generation process of the vortex ring by Steiner *et al.* (2025). The dimensionless coefficients for the circulation c_Γ and the core radius c_a, defined as

$$c_\Gamma = \frac{|\Gamma|}{L^{4/3} D^{2/3} \tau^{-1}} \quad \text{and} \quad c_a = \frac{a}{L^{2/3} D^{1/3}}, \tag{A4}$$

have been shown to depend on the two ratios b/D and L/D for close-wall motions, rather than being constant for far-wall motions, and to differ between the approaching and leaving cases, as detailed in the following.

https://doi.org/10.1017/jfm.2026.11597 Published online by Cambridge University Press

b (cm)	L (cm)	D (cm)	τ (s)	L/D	b/D	Re	Symbols
0.2	2–5.2	5–15	0.5–0.52	0.19–0.56	0.013–0.04	$1.3\times10^3-8.8\times10^3$	△/▲
0.5	2–5.2	10	0.5–2.5	0.2–0.52	0.05	$1.8\times10^3-8.8\times10^3$	▽/▼
1	2–5.2	5–15	0.5–2.5	0.19–0.56	0.067–0.2	$1.8\times10^3-9.8\times10^3$	♦/♦
1.5	2–5.2	10	0.5–2.5	0.2–0.52	0.15	$1.8\times10^3-1.3\times10^4$	○/●
2	2–5.2	7.5–15	0.36–0.83	0.19–0.52	0.13–0.27	$5.3\times10^3-2\times10^4$	□/■
0.2–13	2.8– 11.2	10–40	0.5	0.28	0.005–1.3	1.5×10^4	◀
0.4–2	2–16	8–40	0.5	0.05–2	0.05	1.5×10^4	▶
20	2–20	3.75–40	0.25–2.5	0.07–2	0.5–5.3	$10^3-3\times10^4$	○/●

Table 2. Sets of experimental and numerical parameters, associated non-dimensional numbers, and corresponding symbols used for figure 15. Empty symbols correspond to experiments and full symbols correspond to numerical simulations.

A.2.1. *Vortex scalings in the approaching case*

When the disk is translating towards the wall, the dimensionless coefficients for the maximum circulation c_{Γ_m} and the maximum radius c_{a_m} of the vortex core have been shown by Steiner *et al.* (2025) to follow the scalings

$$c_{\Gamma_m} \simeq \begin{cases} 2.1 \\ \\ 1.3\,(L/D)^{-0.1}(b/D)^{-0.28} \end{cases} \quad \text{for} \quad (L/D)^{-0.1}(b/D)^{-0.28} \begin{cases} \lesssim 1.6, \\ \\ \gtrsim 1.6, \end{cases} \tag{A5}$$

$$c_{a_m} \simeq \begin{cases} 0.1 \\ \\ 6.8\times10^{-2}(L/D)^{-0.12}(b/D)^{-0.14} \end{cases} \quad \text{for} \quad (L/D)^{-0.12}(b/D)^{-0.14} \begin{cases} \lesssim 1.4, \\ \\ \gtrsim 1.4. \end{cases} \tag{A6}$$

The maximum circulation Γ_m and core radius a_m of the starting vortex in the near-wall configuration for the approaching case can be rewritten in dimensional form as

$$|\Gamma_m| \simeq 1.3\,L^{1.23}D^{1.05}b^{-0.28}\tau^{-1} \quad \text{and} \quad a_m \simeq 6.8\times10^{-2}L^{0.55}D^{0.59}b^{-0.14}. \tag{A7}$$

The circulation Γ_1 and core radius a_1 of the starting vortex ring at the disk stop ($t^*=1$) have not been reported by Steiner *et al.* (2025), but Steiner (2023) has shown that they follow the same scalings as the maximum values with only slightly smaller coefficients:

$$c_{\Gamma_1} \simeq \begin{cases} 1.9 \\ \\ 1.1\,(L/D)^{-0.1}(b/D)^{-0.28} \end{cases} \quad \text{for} \quad (L/D)^{-0.1}(b/D)^{-0.28} \begin{cases} \lesssim 1.7, \\ \\ \gtrsim 1.7, \end{cases} \tag{A8}$$

$$c_{a_1} \simeq \begin{cases} 0.085 \\ \\ 6.4\times10^{-2}(L/D)^{-0.12}(b/D)^{-0.14} \end{cases} \quad \text{for} \quad (L/D)^{-0.12}(b/D)^{-0.14} \begin{cases} \lesssim 1.3, \\ \\ \gtrsim 1.3. \end{cases} \tag{A9}$$

The measured values for the dimensionless coefficients c_{Γ_1} and c_{a_1} from the PIV experimental measurements (open symbols) and numerical simulations (filled symbols) described by Steiner (2023) are reported in figure 15 for the flow configurations reported in table 2. The circulation Γ_1 and radius a_1 of the starting vortex at the disk stop ($t^*=1$)

https://doi.org/10.1017/jfm.2026.11597 Published online by Cambridge University Press

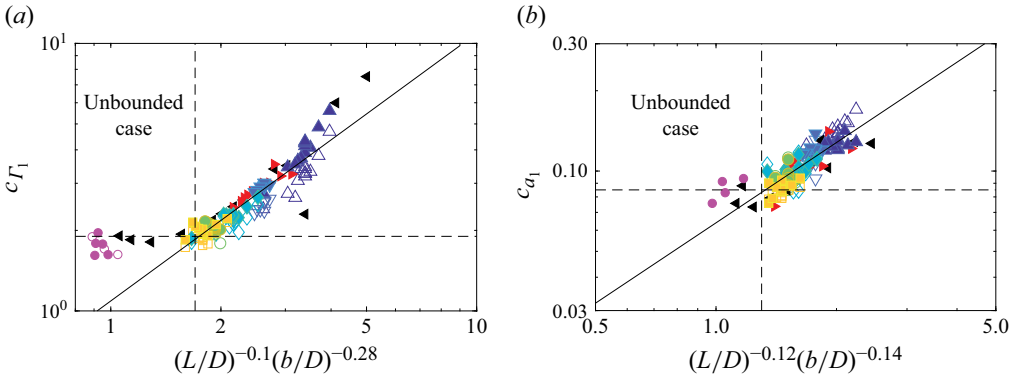


Figure 15. Dimensionless (*a*) circulation c_{Γ_1} as a function of $(L/D)^{-0.1}(b/D)^{-0.28}$ and (*b*) dimensionless core radius c_{a_1} as a function of $(L/D)^{-0.12}(b/D)^{-0.14}$ for a disk moving towards a wall. The horizontal dashed lines are $c_{\Gamma_1,\infty} \simeq 1.9$ and $c_{a_1,\infty} \simeq 0.085$, which correspond to the values obtained in an infinite medium by Steiner *et al.* (2023). The equations of the solid lines are (*a*) $c_{\Gamma_1} = 1.1(L/D)^{-0.1}(b/D)^{-0.28}$ and (*b*) $c_{a_1} = 0.064(L/D)^{-0.12}(b/D)^{-0.14}$. The vertical dashed lines are (*a*) $(L/D)^{-0.1}(b/D)^{-0.28} = 1.7$ and (*b*) $(L/D)^{-0.12}(b/D)^{-0.14} = 1.3$. All the open (respectively filled) symbols correspond to the experiments (respectively simulations) reported in table 2.

in the near-wall configuration for the approaching case can be rewritten in dimensional form as

$$|\Gamma_1| \simeq 1.1\, L^{1.23} D^{1.05} b^{-0.28} \tau^{-1} \quad \text{and} \quad a_1 \simeq 6.4 \times 10^{-2} L^{0.55} D^{0.59} b^{-0.14}. \tag{A10}$$

A.2.2. *Vortex scalings in the leaving case*

When the disk is translating *away* from the wall, the dimensionless coefficient for the maximum circulation c_{Γ_m} of the starting vortex has been shown by Steiner *et al.* (2025) to follow the scalings

$$c_{\Gamma,m} = \begin{cases} 2.1 & \\ 1.13\,(L/D)^{-0.18}(b/D)^{-0.28} & \end{cases} \quad \text{for} \quad (L/D)^{-0.18}(b/D)^{-0.28} \begin{cases} < 1.9, \\ > 1.9. \end{cases} \tag{A11}$$

The maximum circulation Γ_m of the starting vortex in the near-wall configuration for the leaving case can be rewritten in dimensional form as

$$|\Gamma_m| = 1.13\, L^{1.15} D^{1.12} b^{-0.28} \tau^{-1}. \tag{A12}$$

The maximum core radius of the starting vortex for the leaving case has been shown by Steiner *et al.* (2025) to remain unchanged from the unbounded case.

References

Auzerais, A., Jarno, A., Ezersky, A. & Marin, F. 2016 Formation of localized sand patterns downstream from a vertical cylinder under steady flows: experimental and theoretical study. *Phys. Rev. E* **94** (5), 052903.

Badr, S., Gauthier, G. & Gondret, P. 2016 Crater jet morphology. *Phys. Fluids* **28** (3), 033305.

Bethke, N. & Dalziel, S.B. 2012 Resuspension onset and crater erosion by a vortex ring interacting with a particle layer. *Phys. Fluids* **24** (6), 063301.

Brunier-Coulin, F., Cuéllar, P. & Philippe, P. 2017 Erosion onset of a cohesionless granular medium by an immersed impinging round jet. *Phys. Rev. Fluids* **2** (3), 034302.

Buffington, J.M. & Montgomery, D.R. 1997 A systematic analysis of eight decades of incipient-motion studies. *Water Resour. Res.* **33**, 1993–2029.

https://doi.org/10.1017/jfm.2026.11597 Published online by Cambridge University Press

CHARRU, F., ANDREOTTI, B. & CLAUDIN, P. 2013 Sand ripples and dunes. *Annu. Rev. Fluid Mech.* **45**, 469–493.

CHARRU, F., BOUTELOUP, J., BONOMETTI, T. & LACAZE, L. 2016 Sediment transport and bedforms: a numerical study of two-phase viscous shear flow. *Meccanica* **51** (12), 3055–3065.

CHAUCHAT, J., CHENG, Z., HSU, T.-J., CALANTONI, J., ARMENIO, V. & GRECO, M. 2017 Sedfoam-2.0: a 3d two-phase flow numerical model for sediment transport. *Geosci. Model Develop.* **10** (12), 4367–4392.

CHAUCHAT, J. & MÉDALE, M. 2010 A three-dimensional numerical model for incompressible two-phase flow of a granular bed submitted to a laminar shearing flow. *Comput. Meth. Appl. Mech. Engng* **199** (9–12), 439–449.

DU BOYS, P.-F. 1879 Le Rhône et les rivières à lit affouillable. Etude du Rhône et de l'action exercée par les eaux sur un lit à fond de graviers indéfiniment affouillable. *Ann. Ponts Chaussées* **49** (2), 141–195.

EAMES, I. & DALZIEL, S.B. 2000 Dust resuspension by the flow around an impacting sphere. *J. Fluid Mech.* **403**, 305–328.

ELHADIDI, B. & KHALIFA, H.E. 2013 Aerodynamic resuspension of particles due to a falling flat disk. *Particul. Sci. Technol.* **31** (1), 35–44.

FRANKLIN, E.M. 2015 Formation of sand ripples under a turbulent liquid flow. *Appl. Math. Model.* **39** (23–24), 7390–7400.

FRANKLIN, E.M. & CHARRU, F. 2011 Subaqueous barchan dunes in turbulent shear flow. part 1. dune motion. *J. Fluid Mech.* **675**, 199–222.

GARCIA, M.H. 1999 Sedimentation and erosion hydraulics of sediments. *ASCE Manual* **54**, 1–154.

HAGER, W.H. 2005 Du Boys and sediment transport. *J. Hydraul Res.* **43** (3), 227–233.

HANSON, G.J. & COOK, K.R. 2004 Apparatus, test procedures, and analytical methods to measure soil erodibility in situ. *Appl. Engng Agric.* **20** (4), 455–462.

IVERSEN, J.D. & WHITE, B.R. 1976 Saltation threshold on Earth, Mars and Venus. *Sedimentology* **23**, 433–449.

KHALIFA, H.E. & ELHADIDI, B. 2007 Particle levitation due to a uniformly descending flat object. *Aerosol Sci. Technol.* **41** (1), 33–42.

KUBOTA, Y., HALL, J.W. & HIGUCHI, H. 2009 An experimental investigation of the flow field and dust resuspension due to idealized human walking. *J. Fluids Engng* **131** (8), 081104.

KUBOTA, Y. & HIGUCHI, H. 2013 Aerodynamic particle resuspension due to human foot and model foot motions. *Aerosol Sci. Technol.* **47** (2), 208–217.

LA RAGIONE, L., LAURENT, K., JENKINS, J.T. & BEWLEY, G.P. 2019 Bedforms produced on a particle bed by vertical oscillations of a plate. *Phys. Rev. Lett.* **123**, 058501.

LACHAUSSÉE, F., BERTHO, Y., MORIZE, C., SAURET, A. & GONDRET, P. 2018 Competitive dynamics of two erosion patterns around a cylinder. *Phys. Rev. Fluids* **3** (1), 012302(R).

LAJEUNESSE, E., MALVERTI, L. & CHARRU, F. 2010 Bed load transport in turbulent flow at the grain scale: experiments and modeling. *J. Geophys. Res. Earth Surf.* **115** (F4).

LOISELEUX, T., GONDRET, P., RABAUD, R. & DOPPLER, D. 2005 Onset of erosion and avalanche for an inclined granular bed sheared by a continuous laminar flow. *Phys. Fluids* **17** (10), 103304.

MANES, C. & BROCCHINI, M. 2015 Local scour around structures and the phenomenology of turbulence. *J. Fluid Mech.* **779**, 309–324.

MARTINO, R., TORIGGIA, I., PATERSON, A. & PIVA, M. 2018 To-and-fro motion of a submerged plate above an erodible bed. *Environ. Fluid Mech.* **18** (4), 787–805.

MASUDA, N., YOSHIDA, J., ITO, B., FURUYA, T. & SANO, O. 2012 Collision of a vortex ring on granular material. Part I. Interaction of the vortex ring with the granular layer. *Fluid Dyn. Res.* **44** (1), 015501.

MILLER, M.C., MCCAVE, I.N. & KOMAR, P.D. 1977 Threshold of sediment motion under unidirectional currents. *Sedimentology* **24**, 507–527.

MUNRO, R.J., BETHKE, N. & DALZIEL, S.B. 2009 Sediment resuspension and erosion by vortex rings. *Phys. Fluids* **21**, 046601.

MÄDLER, L. & KOCH, W. 1999 Particle resuspension burst from dust layers induced by impacting objects. *J. Aerosol Sci.* **30**, S731–S732. Proceedings of the 1999 European Aerosol Conference.

OURIEMI, M., AUSSILLOUS, P., MEDALE, M., PEYSSON, Y. & GUAZZELLI, E. 2007 Determination of the critical shields number for particle erosion in laminar flow. *Phys. Fluids* **19** (6), 061706.

QUIBEUF, G., CHARRU, F. & LACAZE, L. 2020 Particle motion within the viscous sublayer of a turbulent shear flow. *Phys. Rev. Fluids* **5** (1), 014306.

ROULUND, A., SUMER, B.M., FREDSØE, J. & MICHELSEN, J. 2005 Numerical and experimental investigation of flow and scour around a circular pile. *J. Fluid Mech.* **534**, 351–401.

SAJADI, B., SAIDI, M.H., AHMADI, G., KENNEY, S.M. & TAYLOR, J. 2013 On the induced airflow and particle resuspension due to a falling disk. *Particul. Sci. Technol.* **31** (2), 190–198.

https://doi.org/10.1017/jfm.2026.11597 Published online by Cambridge University Press

SALEVAN, J.C., CLARK, A.H., SHATTUCK, M.D., O'HERN, C.S. & OUELLETTE, N.T. 2017 Determining the onset of hydrodynamic erosion in turbulent flow. *Phys. Rev. Fluids* **2** (11), 114302.

SHARMA, R.S., GONG, M., AZADI, S., SAURET, A. & GONDRET, P. 2022 Erosion of cohesive grains by an impinging turbulent jet. *Phys. Rev. Fluids* **7**, 074303.

SHIELDS, A. 1936 Application of similarity principles and turbulence research to bed-load movement. *Mitt. der Preussischen Versuchsanstalt für Wasserbau* **26**, 1–26.

STEINER, J. 2023 Anneaux tourbillonnaires et érosion dans le sillage d'un disque en translation. PhD thesis, Université Paris-Saclay.

STEINER, J., MORIZE, C., DELBENDE, I., SAURET, A. & GONDRET, P. 2023 Vortex rings generated by a translating disk from start to stop. *Phys. Rev. Fluids* **8**, 064702.

STEINER, J., MORIZE, C., DELBENDE, I., SAURET, A. & GONDRET, P. 2025 Vortex ring induced by a disk translating toward or away from a wall. *Phys. Rev. Fluids* **10** (8), 084704.

WHITE, C.M. 1940 The equilibrium of grains on the bed of a stream. *Proc. R. Soc. Lond. A* **174**, 322–338.

WILLIAMSON, C.H.K. & ROSHKO, A. 1988 Vortex formation in the wake of an oscillating cylinder. *J. Fluids Struct.* **2**, 355–381.

WINTER, A.G., DEITS, R.L.H. & HOSOI, A.E. 2012 Localized fluidization burrowing mechanics of *Ensis directus*. *J. Expl Biol.* **215**, 2072–2080.

YOSHIDA, J. & SANO, O. 2014 Erosion of the granular layer due to the collision of a vortex ring. *Fluid Dyn. Res.* **46**, 061421.

ZHANG, X., AHMADI, G., QIAN, J. & FERRO, A. 2008 Particle detachment, resuspension and transport due to human walking in indoor environments. *J. Adhes. Sci. Technol.* **22** (5–6), 591–621.

https://doi.org/10.1017/jfm.2026.11597 Published online by Cambridge University Press